Estuarine, Coastal and Shelf Science (1989) **28**, 615–638

Turbulent Momentum and Salt Transport in the Mixing Zone of the Elbe Estuary

M. Schröder[a] and G. Siedler

Institut für Meereskunde, Kiel, F.R. Germany

Received 18 April 1988 and in revised form 11 January 1989

Keywords: turbulence spectra; eddy viscosity; eddy diffusivity; acoustic turbulence meters; tidal flow; mixing zone; Elbe estuary

Measurements in the mixing zone of the Elbe estuary were performed during three consecutive tidal cycles with three types of instruments—a moored tripod with velocity and temperature/conductivity/light attenuation sensors, a profiling sonde with similar sensors lowered from an anchored vessel, and instrumented moorings. Acoustic-travel-time sensors were used for velocity measurements.

Spectral analysis of 12·8 min pieces of the obtained time series gives results that are consistent with isotropic turbulence for part of the frequency space. Temporal changes of turbulent kinetic energy are correlated with tidal current velocity. A retardation is found between changes in tidal current and turbulent energy. Not all shear stress terms are in similar phase with tidal flow. Mean gradients, Reynolds stress terms, and turbulent salt flux terms are combined to determine eddy viscosity and eddy diffusion coefficients.

Introduction

Determinations of the turbulent flow fields in estuaries by traditional techniques using mechanical sensors or hot-wire/hot-film anemometers are impeded by the plant and particle loads of such waters. Successful measurements in estuaries have been performed with electromagnetic sensors (Bowden & Howe, 1963; Soulsby, 1977; Anwar & Atkins, 1980; Shiono, 1981; Flügge, 1982) and with acoustic Doppler systems (Wiseman, 1969; Seitz, 1973). We have used acoustic-travel-time current meters to observe the turbulent flow field in the Elbe estuary. Simultaneous hydrographic and water level measurements allowed us to relate variations in the structures of turbulence and kinetic energy to tidal current changes. The aims of this study were to:

— test the suitability of acoustic-travel-time current sensors for measuring turbulent fluctuations in estuaries;
— obtain information on spectral properties of the turbulent field in the Elbe estuary;
— determine the tidal changes of turbulent-shear-stress terms in the mixing zone;
— establish the relationship between changes of the mean flow and turbulent energy; and
— determine eddy diffusion and viscosity coefficients by using the gradient method.

[a]Present address: Alfred-Wegener-Institut für Polar- und Meeresforschung, Bremerhaven, F.R. Germany.

0272–7714/89/060615 + 24 $03.00/0

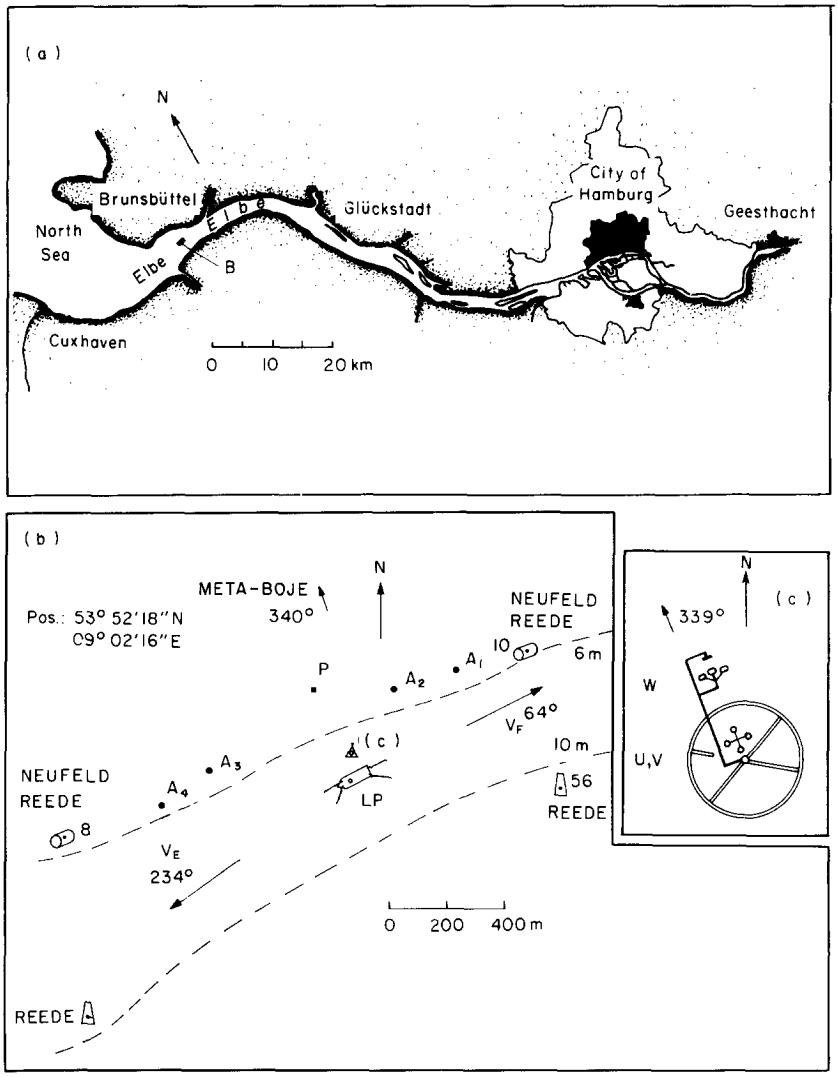

Figure 1. Map of the Elbe estuary (a) and of the observational site (b). The site is also indicated by B in (a). Indicated in (b): LP = moored research vessel LUDWIG PRANDTL, triangle = tripod, A_1 to A_4 = current meter moorings, P = pressure tide gauge, V_E = mean ebb current direction., V_F = mean flood current direction. The orientation of the acoustic current component sensors on the tripod is given in (c).

We begin with background information on the topography and typical hydrographic conditions in the Elbe estuary, followed by a description of the data set and the results of the analysis.

Topography and hydrography of the Elbe estuary

The Elbe estuary reaches from the North Sea coast up to the Geesthacht dam, a distance of approximately 140 km (Figure 1a). Its width changes from ~15 km at the coast to ~1 km inland. Between the city of Hamburg and the North Sea, a channel with depths exceeding 10 m and a width of about 1·2 km is located near the southern river bank, providing the

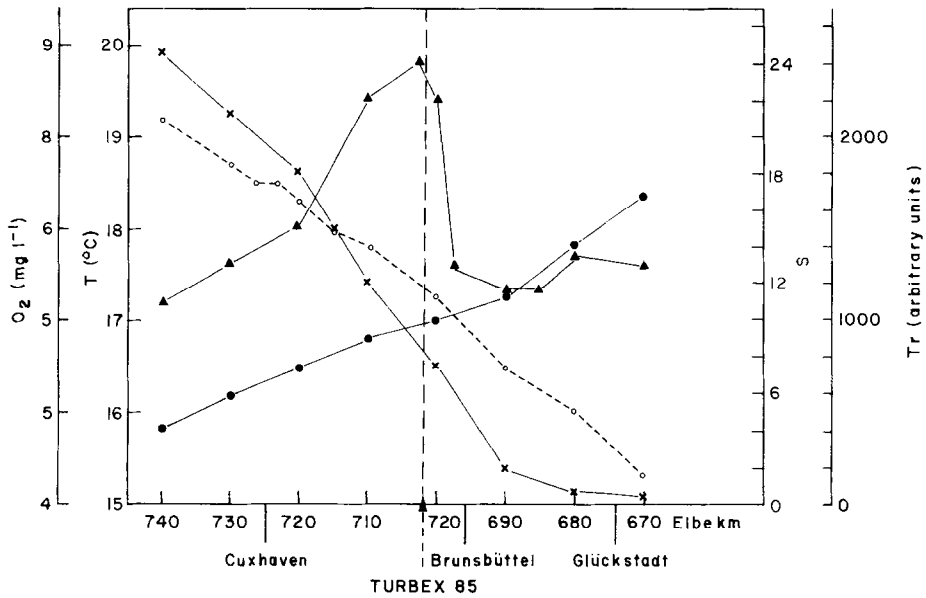

Figure 2. Oxygen O_2 (○), temperature T (●), salinity S (×) (practical salinity units) and turbidity Tr (▲) along the river axis in the mixing zone of the Elbe estuary (after Lucht, 1964; ARGE Elbe, 1986).

main waterway to the city's port. The maximum depth is ~16 m. To the north of this channel, an area with typical depths of 6 to 10 m rises to tidal flats that fall dry at low water time. The observation site, a strip ~1 km long parallel to the river axis, was selected near km 702 (as measured from the river source), between the towns of Brunsbüttelkoog (km 695) and Cuxhaven (km 710). The site is indicated by the letter B in Figure 1a and is shown in detail in Figures 1b and 1c. An important consideration in selecting the site was the requirement to anchor the observational platform, research vessel *Ludwig Prandtl*, well away (1 km) from the main waterway. In this area, the bottom is almost flat with a solid sand cover and mean grain size of 0·2 mm. Mean water depth is 7 m relative to Mean Spring Low Water (MSPLW), the semi-diurnal tidal range is 3 m, and tidal currents alternate in direction by almost 180°.

The mean fresh water run-off of the Elbe river (1926–1983) near Neu Darchau (km 535·8) varies from 450 $m^3 s^{-1}$ m in summer to 1120 $m^3 s^{-1}$ in winter (ARGE Elbe, 1986), but extreme values of as low as 130 $m^3 s^{-1}$ and as high as 3800 $m^3 s^{-1}$ have been observed (Siefert, 1975; Rohde, 1971). The mixing zone, i.e. the region having the largest horizontal salinity gradients, maximum turbidity, and large particle load is found between the towns of Glückstadt and Cuxhaven (Figure 2). This zone migrates over a range of 40 km along the estuary. The selected site is close to the center of the range occupied by the mixing zone, and has a typical run-off of 500 $m^3 s^{-1}$ in summer, which existed during our observations. Over a semi-diurnal tidal period, conditions at this site change from being well-mixed during most of the time to salinity-stratified for a period of approximately 3 h (Lucht, 1964; Koske et al., 1966).

Measurements and obtained data

Three types of measurements were made during the turbulence experiment in June 1985 (TURBEX 85) (refer to Figure 1b):

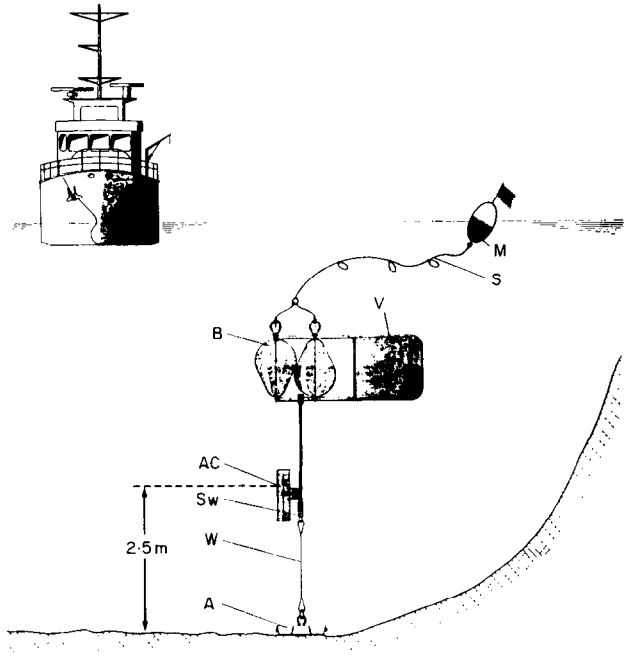

Figure 3. Schematic presentation of the mooring assembly. Indicated: M = marker buoy, S = rope, B = buoyancy, V = vane, AC = Aanderaa Current Meter, SW = swivel, W = wire, A = anchor.

— Ship-board observations with a fast-response profiling instrument on the research vessel *Ludwig Prandtl*, which was fixed in position by 4 anchors at km 702;
— observations with fast-response probes mounted on a tripod (modified after Schauer, 1987) placed on the bottom; and
— slow-response current meter observations at four moorings.

At the beginning of the experiment the four moorings A1 to A4 were deployed on a line parallel to the isobaths at 5·5 m depth below MSPLW (Figure 1b). Each one carried an Aanderaa RCM-4/s current/temperature/conductivity meter at 2·5 m above the bottom (Figure 3). The mooring configuration was tested before the field experiment in strong turbulent flow in a tank at the Research Center Geesthacht. The sampling interval was set at 2 min. On position P (see Figure 1b) a self-recording Aanderaa pressure gauge was also deployed. The moorings were recovered after the end of all the other measurements.

A tripod with a height of 1·62 m was placed mid-way between moorings A1 and A4 at a depth of 7 m (MSPLW). It carried two 2-component ultrasonic current sensors, one measuring two horizontal components 2·58 m above the bottom and the other the vertical and one horizontal component 2·14 m above the bottom (Figure 4). Prior to the experiment the current sensors were tested extensively in a tow tank (for details see Schröder, 1987). The tripod array also included a temperature, a conductivity and a pressure sensor (Kroebel *et al.*, 1976) plus sensors for tripod inclination and orientation with respect to north. The orientation of the current sensor coordinates is indicated in Figure 1c. The horizontal components were measured approximately along and normal to the mean current direction. The data were transferred through a telemetry unit on the tripod and an 80 m long single-conductor cable to the anchored research vessel (Biermann *et al.*, 1976).

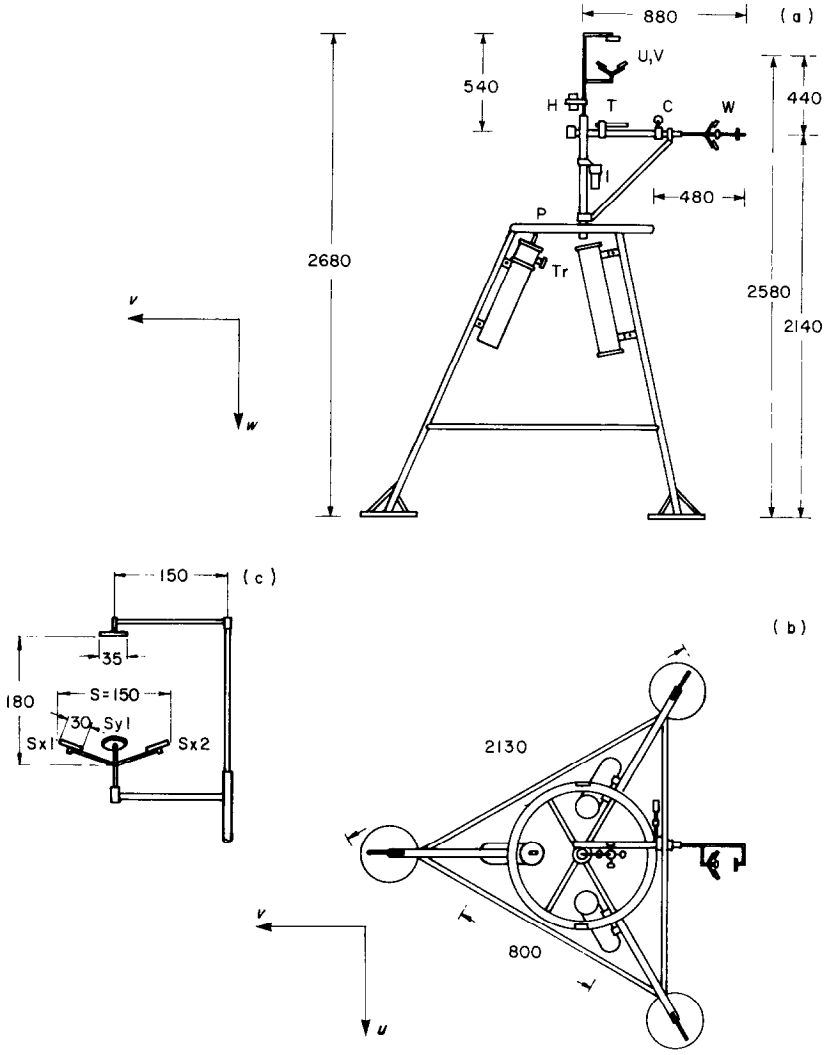

Figure 4. Tripod assembly with tripod lateral view (A), tripod plan view (B) and current sensor assembly lateral view (C). Indicated: U, V, W = current component sensors, T = temperature sensor, C = electrical conductivity sensor, I = inclination sensor, H = heading sensor, P = pressure sensors, Tr = turbidity sensor. Measurements are given in mm.

Magnetometer data providing information on the orientation of the tripod were used to calculate the components in the two preferred directions.

For the ship-board observations a profiling sonde was used (Fanger *et al.*, 1979) which contained similar sensors for two horizontal current components, temperature, conductivity, pressure, and a device for the measurement of optical attenuation (Figure 5). A vane ensured the orientation of the current sensor components along and normal to the mean current direction. Data from both the ship-operated sonde and the tripod were recorded onboard the vessel at a rate of 8 Hz. Lowering the sonde at a speed of $\sim 0{\cdot}2$ m s^{-1} resulted in a vertical resolution of 2 cm. The data were averaged over 20 cm, and the resulting smoothed profiles were then used in the analysis.

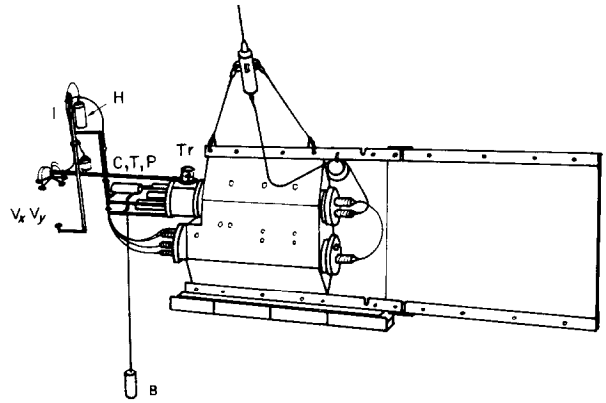

Figure 5. Profiling sonde. Indicated: V_x, V_y = horizontal current component sensors, I = inclination sensor, H = heading sensor, C = electrical sensor, Tr = turbidity sensor, B = bottom sensing weight.

The entire observation period was 35 h, from 26 June 1985, 17·00, to 28 June 1985, 04·00 h, thus spanning approximately three semi-diurnal tidal periods. The planned sampling scheme included repeated sets of 30 min of measurements and 5 min of system checks on the tripod, with vertical profile measurements from the ship at the beginning of the 30 min periods. A total of 54 high-quality profiles and tripod time series were obtained.

The 54 time series were calibrated and plotted for a preliminary quality check, which included examinations for spikes and redundancy of data cycles. Spike elimination poses a serious problem if erroneous values are to be deleted without gravely affecting the high-frequency part of the spectrum. The following method was used. In obviously spike-devoid portions, frequency distributions of differences between consecutive values were determined to obtain typical changes. All records were then compared with these standard distributions, and parts of records with changes exceeding the set limit were marked and plotted for detailed inspection.

Spikes were then eliminated with a modified median filter technique. Values x_i were removed if they were outside a selected difference bandwidth D for a given window in time, with the window moving along the time series. D was set to 3 standard deviations. The condition for elimination was thus $|X_{i+1} - X_i| > D$ for values with number i and $i+1$. The noisiest record was velocity normal to the mean flow. Here up to 3% of the data points had to be rejected in 85% of the total number of time series. In all other cases, the elimination rate was well below 1%.

Examples of quality-checked records are shown in Figure 6. The attenuation coefficient C from the tripod time series compares well with the values from the profiling instrument, given by circles in the lower part of Figure 6. The value of C is a good measure of the suspended matter concentration in such an estuary (Ohm, 1985).

Hydrographic conditions and particle concentration during the tidal cycle

Time series of water depth are presented in Figure 7, together with longitudinal current component (parallel to the isobaths), salinity and attenuation coefficient obtained by the

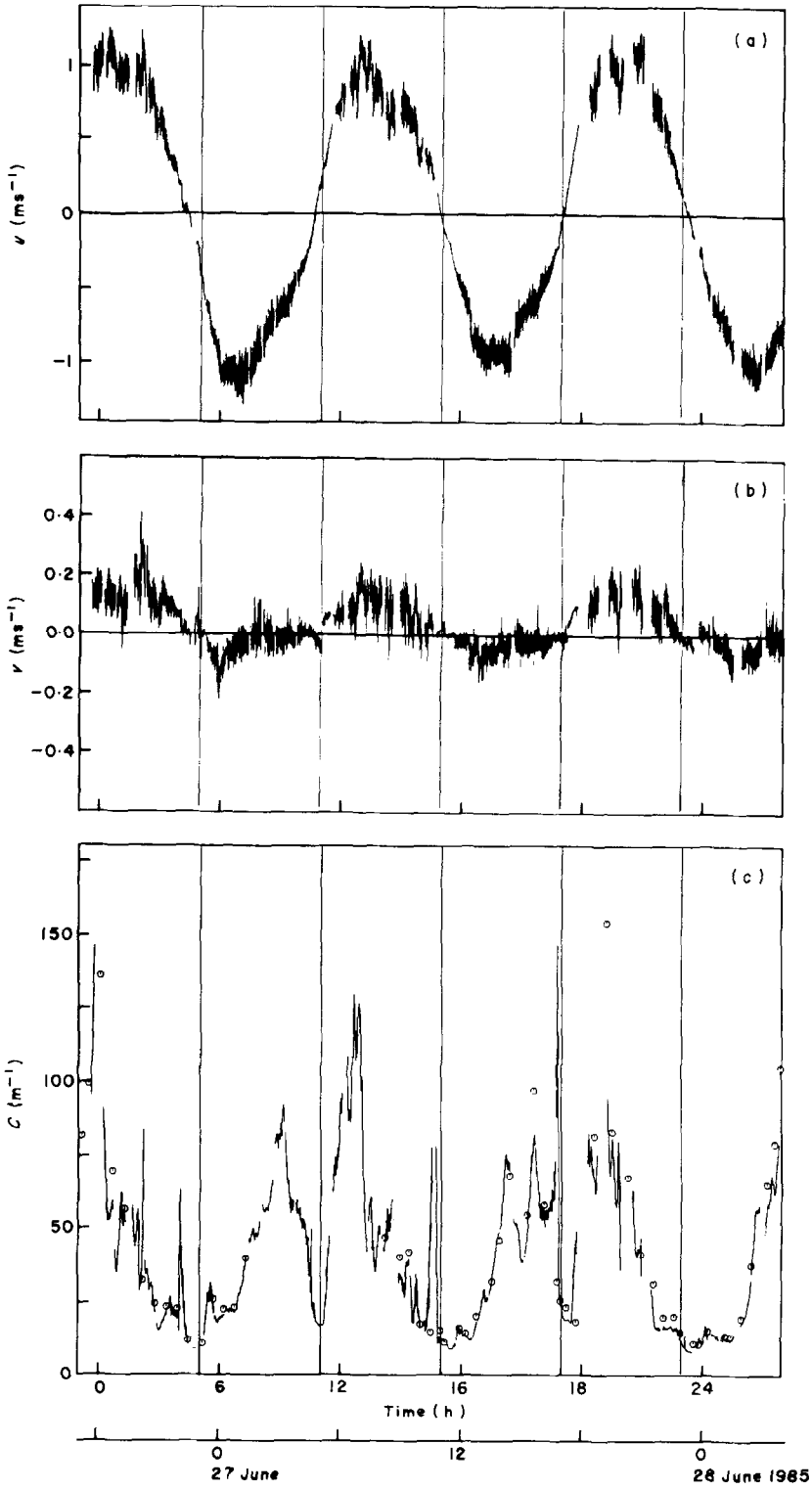

Figure 6. Examples of time series from the tripod. The following variables are presented: u = longitudinal current component (positive: to interior of estuary), v = transverse current component (positive: to the right of the positive u), C = optical attenuation coefficient.

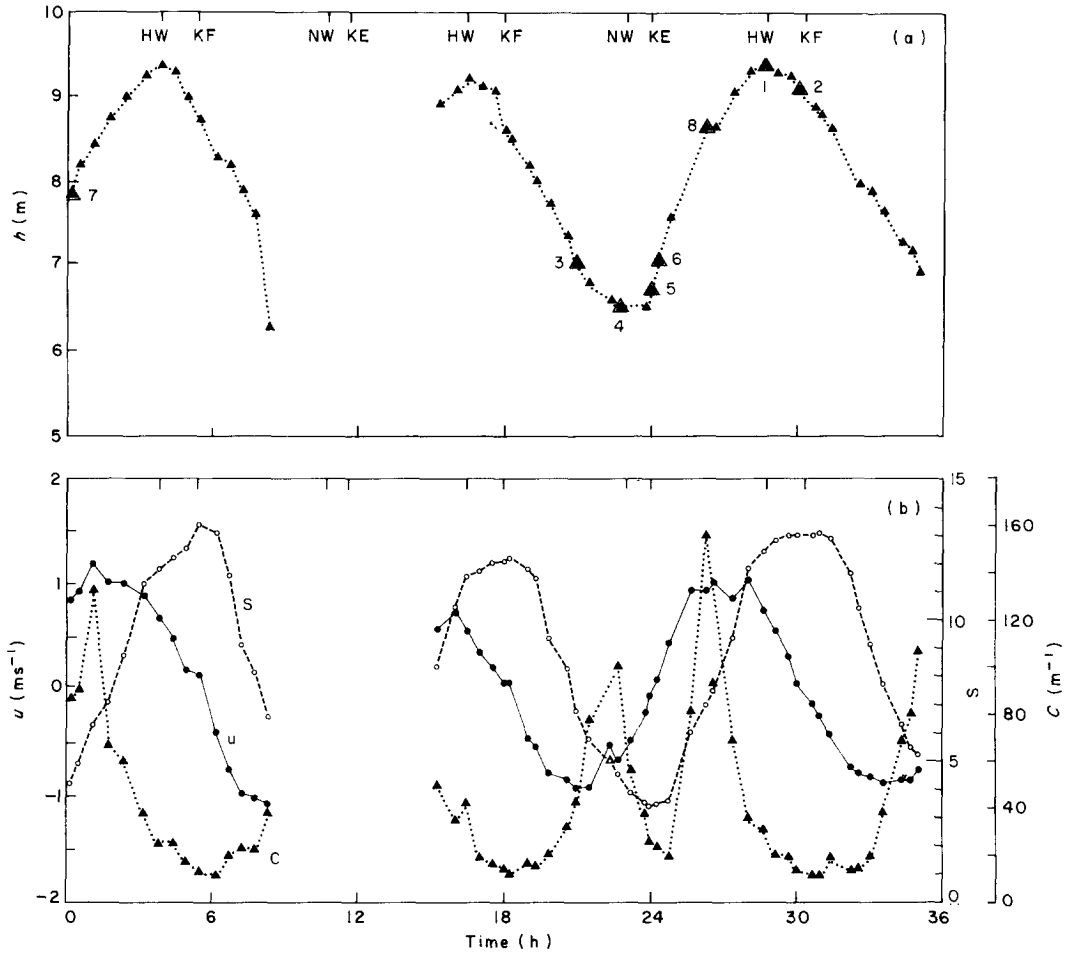

Figure 7. (a) Time series from the profiling sonde of water depth h. (b) Time series at 2·58 m above the bottom of longitudinal current component u, salinity S and optical attenuation coefficient C. Indicated: HW = high water, NW = low water, KF = current turn after flood time, KE = current turn after ebb time.

profiling sonde 2·5 m above the bottom. These series reflect the typical low-frequency variations of the main parameters. Phase differences can be seen between the water level and salinity curves, as well as a delay in slack water occurrence with respect to high and low water. High turbidity values were found near the current maxima, with distinct differences for tidal phases.

Selected vertical profiles are shown in Figure 8. The numbers refer to specific times indicated in Figure 7. According to the salinity curves the water column appears well mixed during most of the tidal cycle except at time no. 2, at slack water after high water, when a 2 m thick low-salinity layer appears at the surface, with a vertical salinity gradient of 4·5 per meter in the halocline. This low value of salinity is probably caused by the advection of low-salinity water across the nearby tidal flats. During most of the tidal cycle turbidity is low, with $C < 20\ m^{-1}$. The current profiles are roughly linear, with typical velocities at flood and ebb time of 0·5 m s^{-1} near the bottom and 1 m s^{-1} near the surface. When velocities in the lower portion of the water column are still decreasing toward zero

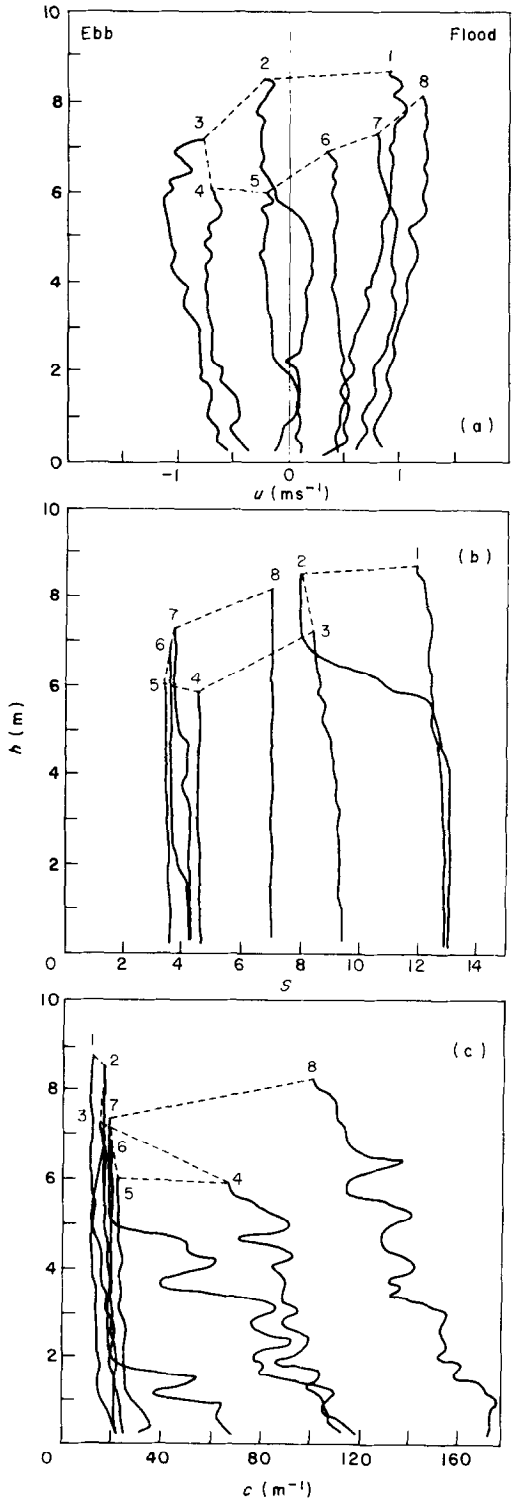

Figure 8. Selected vertical profiles of longitudinal velocity component u, salinity S, and optical attenuation coefficient C *vs.* bottom distance h. The numbers on top of the profiles refer to Figure 7a.

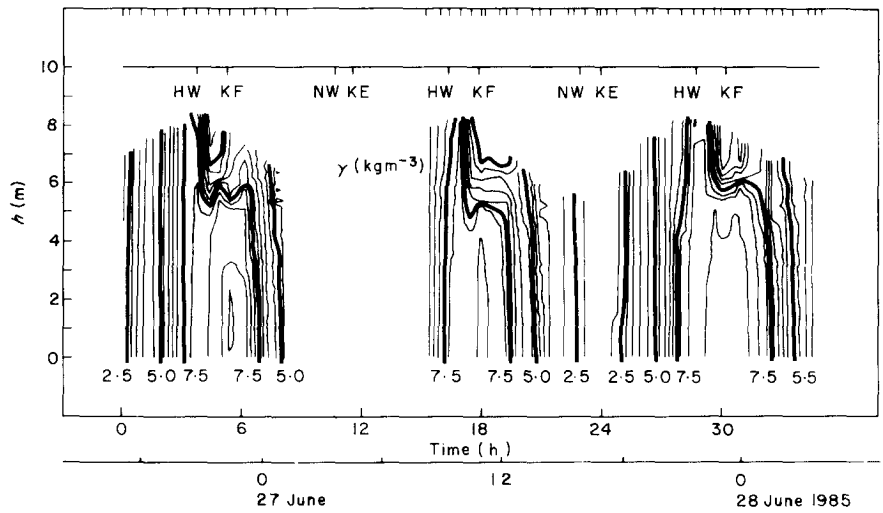

Figure 9. Time series of isopycnal surfaces (γ) *vs.* bottom distance h. For abbreviations see Figure 7.

after flood time (profile no. 2), the velocities in the upper part have already changed to ebb flow, bringing low-salinity water to the observation site. The stratification in salinity is maintained for nearly 3 h after high-water. Apparently, the shear then generates sufficient turbulence to destroy the layer. The resulting density changes are shown in Figure 9.

At low-water conditions a large increase in attenuation is found, with the highest particle concentrations being near the bottom. This time sequence is consistent with the assumption that during the later part of ebb time the near-bottom flow is reduced to a larger extent downstream than upstream, with the resulting convergence concentrating particles in the mixing zone. The majority of particles will be brought to the water column by advection under such conditions and less by material being lifted from the bottom. Such a situation was found during a previous experiment (TURBEX 84) at this location (Riethmüller *et al.*, 1985).

At approximately slack water, after ebb time, the salinity reaches its minimum, and the turbidity suddenly is reduced to low values, indicating an increase in the sedimentation of particles. Some time later, the early flood current brings in high-salinity water and apparently generates greater turbulence, which increases turbidity. The turbidity-increase zone rises from the bottom layer towards the suface. However, maximal values are still seen near the bottom, apparently caused by a resuspension of sediment particles. During this period local mixing processes dominate advection with respect to the influencing particle distributions.

Error estimates

In the following analysis errors will be given in several cases, and uncertainties due to the sampling schemes will be discussed. A detailed error analysis of the data set is given by Schröder (1987), and only a few summarizing comments will be presented here.

The spectral analysis is aimed at identifying the longest interval for which stationarity can be assumed. This necessarily leads to a loss of longer-period information. An

additional error source is given by the sensor dimensions, restricting the spatial resolution at short scales. The path length L of the acoustic-travel-time sensor was 15 cm, about three times the size of the electromagnetic sensors commonly used in estuaries. The measured velocity component represents a spatial mean over the sensor volume multiplied by a weighting function characteristic of the specific sensor. Its spectral transfer function needs to be known, but is not available. Following Soulsby (1980), we used a critical wavelength $\lambda_C \approx 1{\cdot}4 \times L$. After transformation into the frequency domain with mean velocities $0{\cdot}4 < \bar{u} < 1{\cdot}2$ m s^{-1} we obtain a corresponding critical frequency f_c of 1·9 Hz $< f_c <$ 5·7 Hz. These values are consistent with the later results on spectral shapes, with aliasing and noise effects appearing for f > 2 Hz.

Random and systematic errors can be estimated for spectral energies. Assuming normal distributions of velocity fluctuations, the variance in each frequency band can be replaced by the mean spectral density and a compensation bandwidth f_E (Plate, 1974). The mean-square random error E is given by

$$E^2 = \frac{1}{f_E \cdot T} = \frac{\tau_0}{T} \tag{5}$$

where T is record length and τ_0 to the first zero-crossing of the autocorrelation function.

The excess and kurtosis of the distribution for the 12·8 min records were sufficiently small to assume a normal distribution. For $\bar{u} > 0{\cdot}4$ m s^{-1}, we find squared random errors of $2\% < e^2 < 15\%$ for u', v' and w'.

Systematic errors generated by the sampling scheme and analysis procedures were estimated by assuming the variance of fluctuations as being the sum of three independent contributions from different wave number ranges (Shiono, 1981):

$$\overline{u_i'^2} = \int_0^{k_L} E^2{}_{u_i}(k)\mathrm{d}k + \int_{k_L}^{k_H} E^2{}_{u_i}(k)\mathrm{d}k + \int_{k_H}^{\infty} E^2{}_{u_i}(k)\mathrm{d}k, \tag{6}$$

where k_L and k_H correspond to the low and high frequency limits in the earlier analysis. With the assumptions that $E_{u_i} = \text{const}$ for $k < k_L$ and that there is negligible energy in the dissipation range above k_H, we obtain (Shiono, 1981):

$$\overline{u_i'^2} = k_L \times E^2{}_{u_i}(k_L) + \int_{k_L}^{k_H} E^2{}_{u_i}(k)\mathrm{d}k + \frac{3}{2} k_H \times E^2(k_H) \tag{7}$$

and

$$\overline{u_i'^2} = E^2{}_L + I^2 + E^2{}_H \tag{8}$$

The terms $E^2{}_L$, I^2 and $E^2{}_H$ represent the corresponding terms in the preceding equation. Calculating $E^2{}_H$ and $E^2{}_L$ for mean tidal conditions ($\bar{u} \approx 0{\cdot}6$ m s^{-1}) relative to the record variance I^2 leads to:

u	$E^2{}_L/I^2$:	51%	$E^2{}_H/I^2$:	14%
v		15%		39%
w		19%		37%

The large error $E^2{}_L$ of the u-component compared to the v- and w-components is caused by the large extension of low-frequency eddies in the longitudinal direction.

Another error source to be considered is the noise level of the acoustic sensor. This was tested in a tow tank where spectra were obtained in non-turbulent water. Noise levels of up to 2×10^{-5} m^2 s^{-1} in spectral energy density and 4×10^{-5} m^2 s^{-2} in energy were measured.

TABLE 1. Stationarity test. Number of runs from data that are larger than the number of critical runs indicates stationarity

Time intervals (min)		6	7	8	9	10	11	12	13	14	15	16	17	18	19	20
Critical runs		3	4	5	6	6	7	8	9	10	11	11	12	13	14	15
Runs from data:																
Period No. 510	$\overline{u}$	3	4	5	7	8	8	9	10	10	10	10	12	12	10	12
	$\overline{u'^2}$	4	6	8	8	8	8	9	9	9	9	6	7	9	10	10
	$\overline{w'^2}$	3	3	4	4	6	6	8	6	6	8	8	8	9	9	9
	$\overline{u'w'}$	4	5	6	6	6	8	9	10	9	9	10	11	11	11	12
Period No. 515	$\overline{u}$	5	6	7	8	9	10	11	12	11	13	15	18	19	20	18
	$\overline{u'^2}$	5	5	6	8	9	10	10	10	11	12	13	12	13	14	18
	$\overline{w'^2}$	3	4	5	6	7	7	9	10	12	13	13	14	12	11	15
	$\overline{u'w'}$	1	3	5	5	7	9	11	14	15	16	16	17	17	18	20

Only for slack-water conditions ($\overline{u} < 0{\cdot}15$ m s^{-1}) and for frequencies $f > 0{\cdot}8$ Hz will the instrumental noise influence the results.

Stationarity and characteristic time scales

The time series obtained here contain a deterministic (tidal) plus a random (turbulent) component. Statistical properties can be determined for limited time intervals if the condition of stationarity is met during these periods. This requires a constant mean and a constant autocorrelation function for each period. In order to obtain the largest interval in which processes can still be considered stationary, a run-test was performed (Bendat & Piersol, 1971; Soulsby, 1980). It is required that the trend in the selected interval is much smaller than the stochastic fluctuations.

First, the time series were divided into 30 s intervals, trends were removed, and the data were averaged. Such an averaging interval is generally larger than the integral time scale of velocity fluctuations, so the mean values can be regarded as statistically independent. From the centre of a 30 min period, intervals were selected having durations of 6–25 min in increments of 1 min. For each interval a run-test was performed: the mean was subtracted and the number of zero-crossings of the remaining series was determined.

The results of the run-test for various sequences are presented in Table 1. Period No. 515 is typical for ebb conditions, period No. 510 for the time following slack-water after flood. The condition that the number of zero crossings exceeds the number of critical runs is usually met for intervals up to 12–13 min. Although this condition is not fulfilled for all parameters near slack water, this interval is considered a reasonable choice for the following spectral analysis. Similar intervals were used by other investigators: 5 and 10 min by Shiono (1981), 12 min by Soulsby (1980), 10 min by Gross (1984) and 15 min by Grant *et al.* (1962).

The autocorrelation function R_{xx} was computed for two reasons. It permits a separation of deterministic (periodic) and random (turbulent) signals, and it allows for the determination of the integral time scale associated with turbulence. The autocorrelation coefficient r, as a normalized function, is given by:

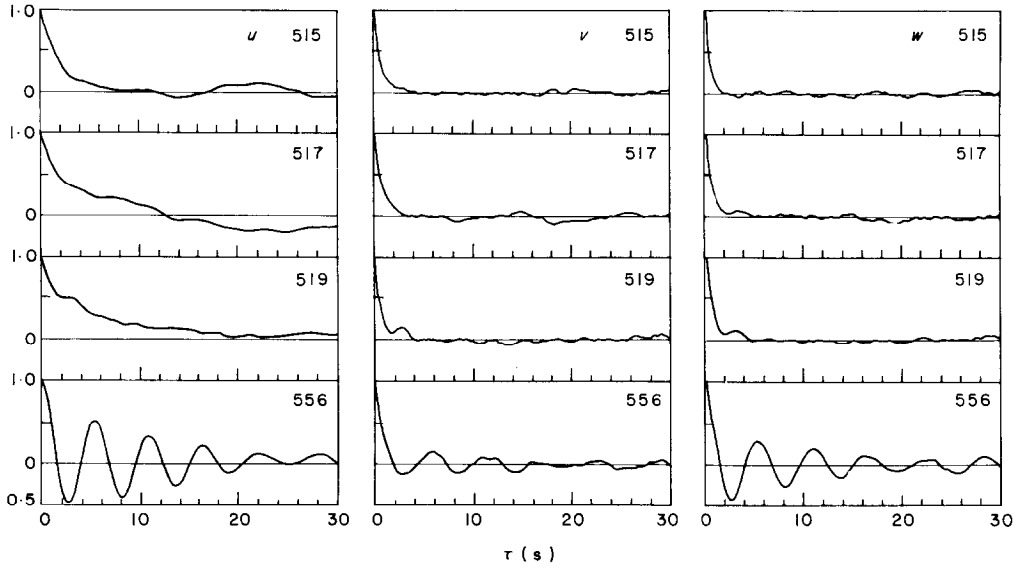

Figure 10. Examples of the normalized autocorrelation function r for velocity components u, v, w versus time lag τ. Typical distributions are given by No. 515 and 517, while No. 519 is an example for the specific period after ebb flow, and No. 556 represents a case with a strong surface wave signal.

$$r(\tau)=\frac{R_{xx}(\tau)}{R_{xx}(O)}, \tag{1}$$

where $R_{xx}(\tau)=\lim_{T\to\infty}\frac{1}{T}\int_0^T x(t)\times(t+\tau)\mathrm{d}t$

and $R_{xx}(0)=\lim_{T\to\infty}\frac{1}{T}\int_0^T x^2(t)\mathrm{d}t.$

Values of $r(\tau)$ were calculated for record lengths of 12·8 min, corresponding to 6144 data cycles, with $0<\tau<45$ s. Some characteristic examples are presented in Figure 10. In record No. 556 strong periodic component is recognized. It was due to surface waves caused either by wind or by swell from passing ships. More typical are records No. 515 and 517, which show r as decreasing to low values and having well-defined zero-crossings. In the special case of record No. 519 (slack water after ebb flow) the autocorrelation coefficient for longitudinal velocity u does not reach a zero-crossing within the maximum time lag τ of 30 s.

With a well-behaved autocorrelation function, the integral time scale $\mathcal{J}$ of turbulence is obtained from

$$\mathcal{J}=\frac{1}{\sigma_x^2}\int_0^\infty R_{xx}(\tau)\mathrm{d}\tau, \tag{2}$$

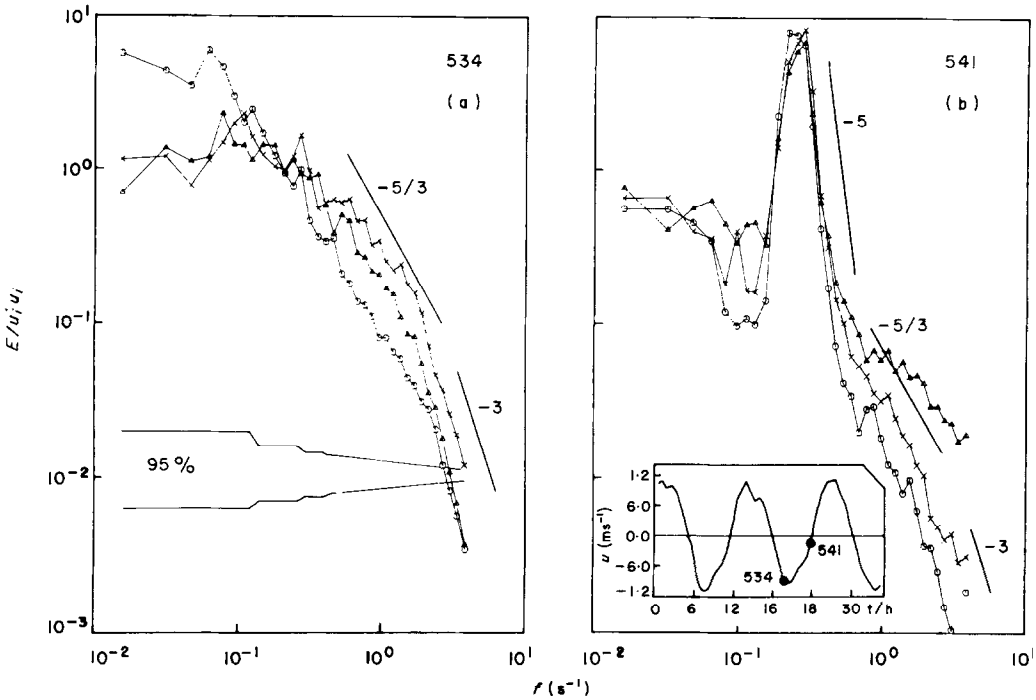

Figure 11. Examples of energy density (E) spectra versus frequency f for cases with maximum tidal current (No. 534, see insert on the right) and with low current (No. 541). Indicated: u = longitudinal velocity component (○), v = transverse velocity component (△), w = vertical current component (×). Numbers at straight lines refer to slopes. The 95% confidence intervals are given on the left.

where σ_x^2 is the variance of the record. The time scales for lateral and vertical velocity components are 5–15 s and 2–8 s, respectively.

Spectral analysis

Energy density spectra were computed using a fast Fourier transform on the 12·8 min records. The 6144 data cycles were cut into 12 segments (64 s) with 512 data points each. The corresponding 256 estimates from each segment were averaged, resulting in a mean spectrum in the frequency range of 0·015–4 s^{-1}. Finally, the values were averaged in such a way as to provide 20 estimates per frequency decade.

Examples of u, v and w spectra, normalized by the mean variance, are presented in Figure 11a for maximum ebb-flow conditions. At low frequencies ($f < 0{\cdot}2$ Hz) spectra are flat, and u-component energy is significantly above the energies of the other two components, whereas vertical velocity is more energetic at higher frequencies. This property is recognized in all spectra with fully developed turbulence in this experiment. It can be explained as being a result of the correlation of pressure and velocity gradient terms in the energy equation (Hinze, 1959). In isotropic turbulent flow, this correlation is responsible for an increase of energy in the cross-stream components owing to along-stream components, mostly at high frequencies (Laufer, 1954). As a result, the degree of isotropy increases and the turbulent shear-stress decreases.

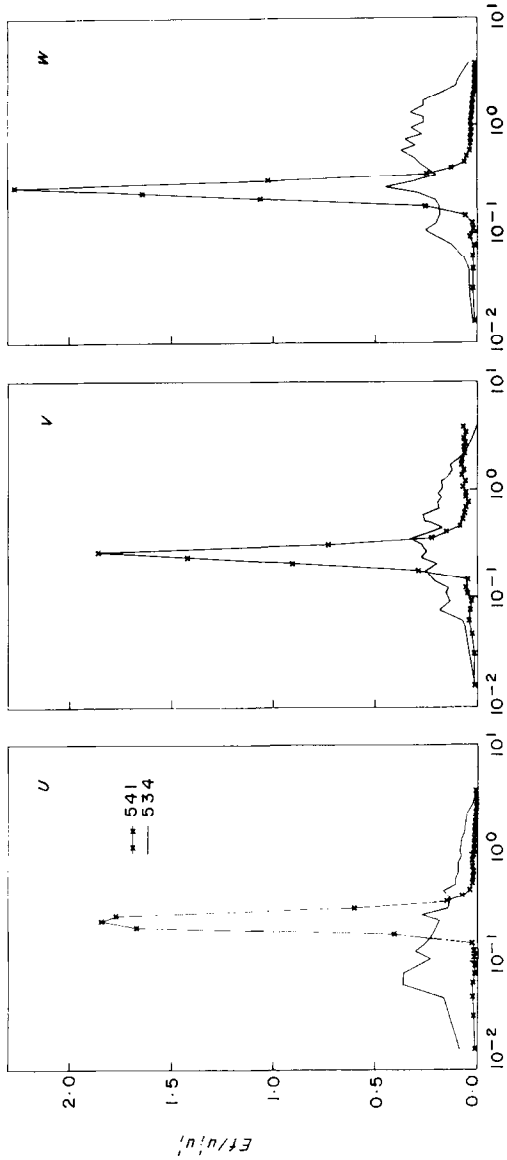

Figure 12. Normalized energy preserving presentation of spectra.

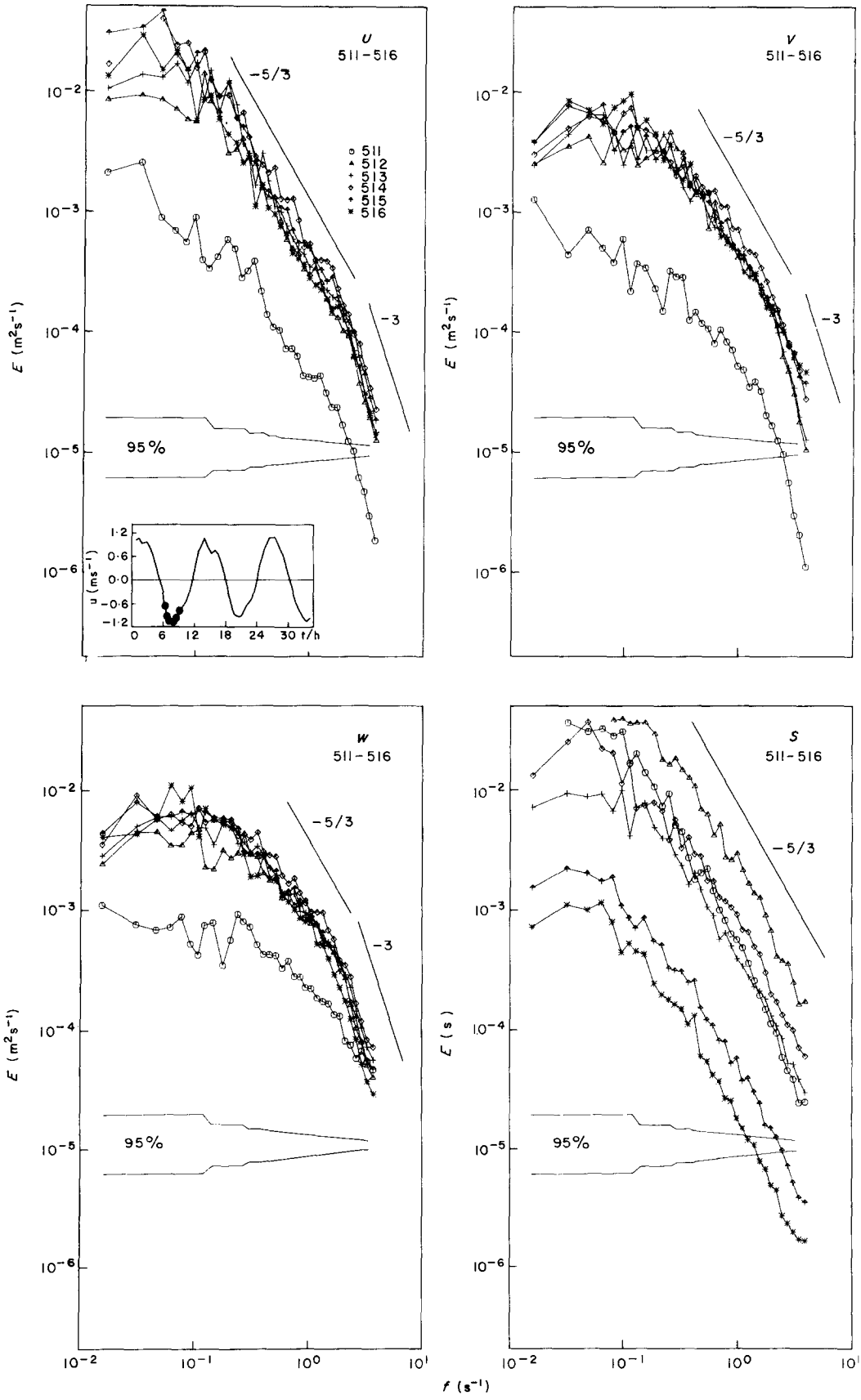
U
511-516
-5/3
-3
95%
511
512
513
514
515
516
u (ms⁻¹)
1·2
0·6
0·0
-0·6
-1·2
0 6 12 18 24 30 t/h
V
511-516
-5/3
-3
95%
W
511-516
-5/3
-3
95%
S
511-516
-5/3
95%
E (m²s⁻¹)
E (s)
f (s⁻¹)
10⁻²
10⁻³
10⁻⁴
10⁻⁵
10⁻⁶
10⁻¹
10⁰
10¹

The slope of $-5/3$, corresponding to the inertial subrange of isotropic turbulence, is indicated in the diagrams. In the frequency range of $0{\cdot}3 < f < 2$ Hz the spectral slopes are well approximated by the $-5/3$ law. The slope of -3, also indicated, was described by Nakagawa *et al.* (1975) as the transition between the inertial and viscous subranges, the later having a slope of -7. At this low-frequency part of the dissipative scales, Inoue (1952) had already demonstrated the -3 dependence, and similar results were obtained by Shiono (1981), whose spectra changed from $-5/3$ to -3 at 1·5 Hz. The spectra in Figure 11b have different properties. A strong maximum is found at 0·2 Hz, with spectral levels being lower at high frequencies. The magnitude of the change in spectral levels between Figure 11a and 11b is demonstrated by the energy-preserving spectra presented in Figure 12.

The mean current velocity was low ($\bar{u} \sim 0{\cdot}12$ m s^{-1}) in the case of Figure 11b, and weak turbulence apparently existed with the weak mean current. The maximum at 0·2 Hz is due to surface waves. The slope of -5, indicated at the high-frequency portion of the peak, is consistent with the results of Philips (1958) and Pierson and Moskowitz (1964) for surface waves and provides additional evidence for a well-behaved current sensor. Observations under similar conditions in the Weser estuary by Barthel (1985) showed a similar energy maximum at $0{\cdot}15 < f < 0{\cdot}4$ Hz. The increase in Figure 11b at $f > 3{\cdot}0$ Hz relative to the -3 slope is due to aliasing and a decreasing signal-to-noise ratio near the Nyquist frequency. This effect is more prominent at slack-water conditions when tubulence levels are generally low.

Similar properties are recognized in the spectra from six consecutive records at ebb tide given in Figure 13, in the absence of surface wave signals. Spectra of $u'w'$, $u'S'$ and $w'S'$ (not shown here) have slopes which are somewhat steeper ($-7/3$) than the spectra in Figure 13.

A cross-sectral analysis was also performed on the data. Except for the cases with strong surface wave signals near 0·2 Hz and cases with small mean currents at the high-frequency end, the coherence levels were below the 95% confidence level for zero coherence. This analysis was used for identifying surface wave signals and is not discussed here.

Dependence of the turbulent stress and salt flux on the tidal cycle

We now consider normal and shear stresses such as $\overline{u'^2}$ and $\overline{u'v'}$, respectively. During ebb tide, we find aproximately:

$$\overline{w'^2} = 1/2(\overline{u'^2} + \overline{v'^2}) \tag{3}$$

Only ebb tide w' data will be used because the sensor mount did impair the flow through the sensor array at flood tide (see Schröder, 1987). Even the ebb tide terms for vertical velocity were somewhat larger than expected. We were not able, however, to identify any instrumental effects that might have caused an increase ony for w'. We will use (3) for obtaining $\overline{w'^2}$ during flood tide.

Figure 13. Examples of energy spectra for cases of lacking surface wave signals and strong tidal currents, given for fluctuations of current components u, v, w, and salinity S. The symbols used in the curves are indicated in the upper left diagram. Slopes of straight lines and 95% confidence intervals are also given.

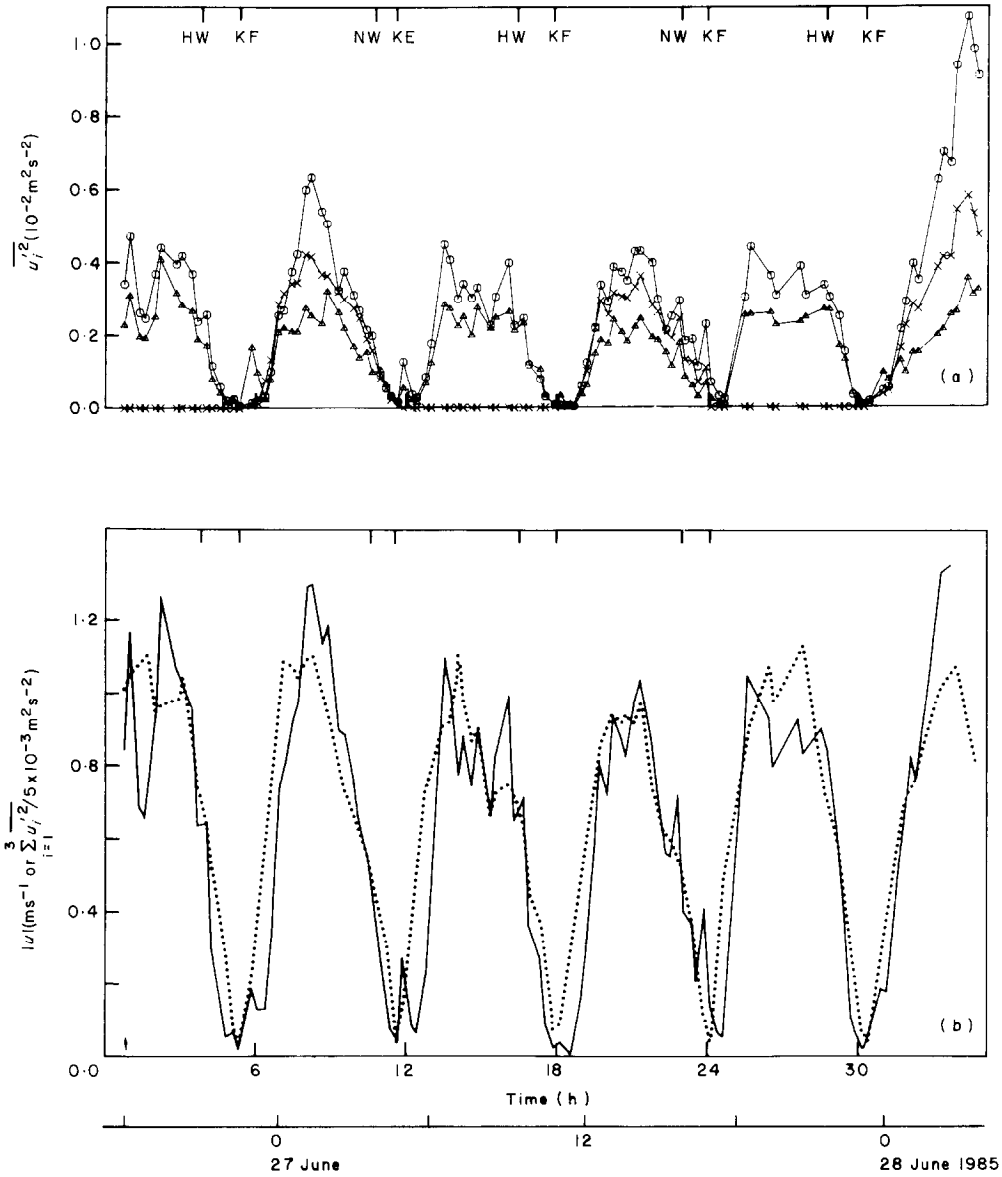

Figure 14. Time series of eddy kinetic energy terms $\overline{u'^2_i}$ (A), absolute value of mean longitudinal current $|u|$ and total eddy kinetic energy $\sum \overline{u'^2_i}$ (B). For abbreviations see Figure 7.

The three normal stress terms, $\overline{u'^2}$, $\overline{v'^2}$ and $\overline{w'^2}$, are presented in Figure 14a, but without $\overline{w'^2}$ for flood time. Half the sum of the three terms, with $\overline{w'^2}$ obtained as explained above, is given in Figure 14b, which represents the total kinetic energy per unit mass of the fluctuating field. The magnitude of the tidal current component is also potted in Figure 14b. It is obvious that the kinetic energy of the fluctuating field is strongly dependent on, and almost in phase with, the tidal current.

Observations by Flügge (1982) in the Weser estuary indicated a retardation of almost one hour in the increase of turbulent kinetic energy after slack water with respect to the

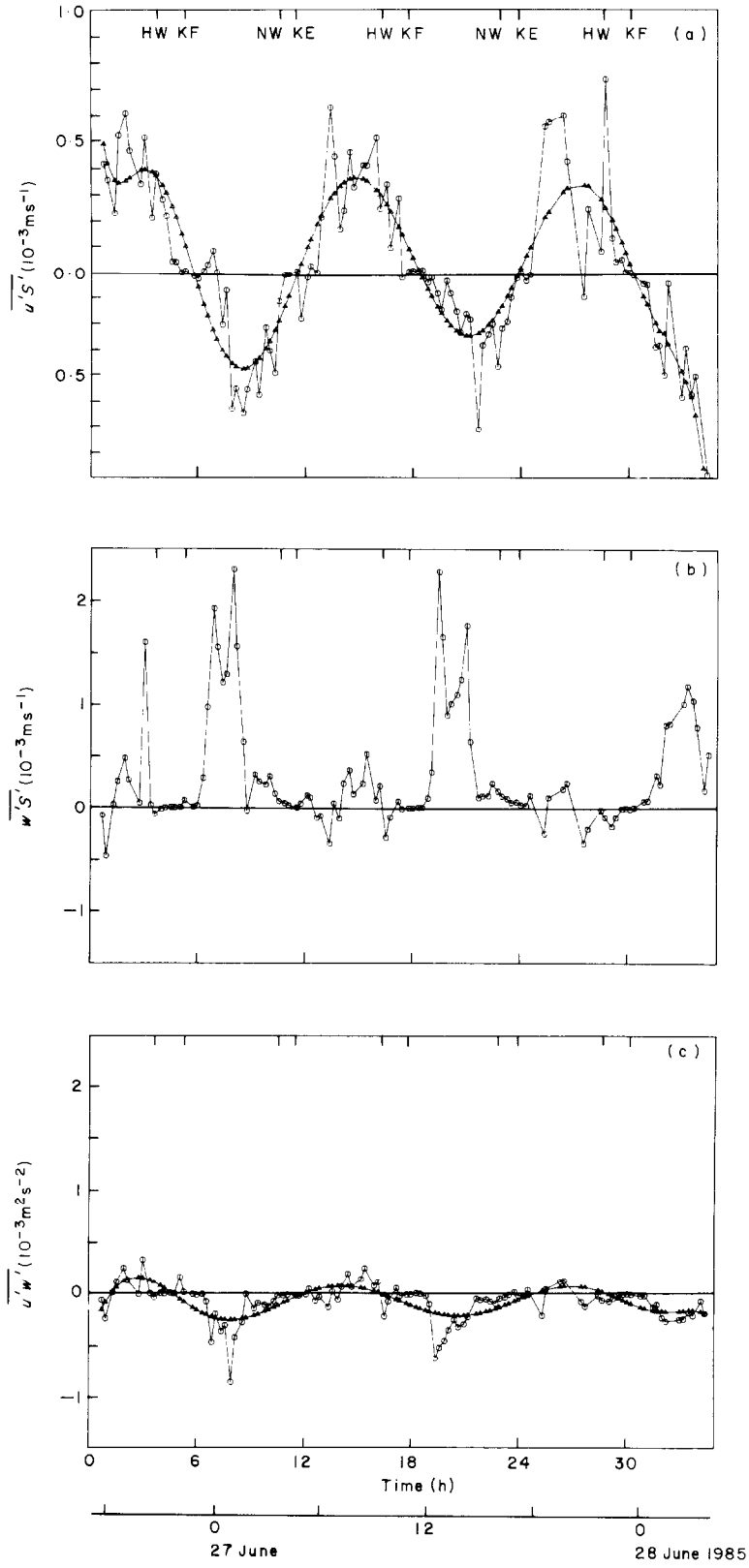

Figure 15. Time series of eddy salt transport terms $\overline{u'S}$, $\overline{w'S'}$ (a, b) and shear stress term $\overline{u'w'}$ (c), with data (○) and fit (▲) indicated in lower diagram. For abbreviations see Figure 7.

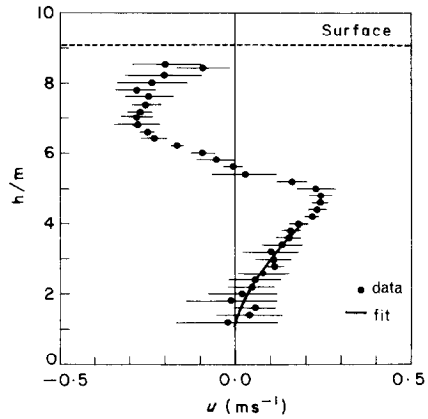

Figure 16. Example of longitudinal current (u) profile *vs.* bottom distance h, with averages from up and down profile (●) and variance (horizontal thin lines). At h = 1–4 m the polynomial fit is given by the heavy line (——).

tidal current increase. The present study leads to a similar result for the first four slack-water periods. The effect is apparently caused by the time needed after slack water for the shear in the increasing current to generate turbulent motions. However, during the final slack-water period the retardation cannot be seen. Nearing the end of the experiment, strong westerly winds arose that generated waves and turbulence, which acted to obscure the retardation.

The shear stress terms are only partly dependent on the tidal cycle. While $\overline{u'v'}$ and $\overline{v'w'}$ do not change systematically with the tidal cycle, the term $\overline{u'w'}$ does. This last term, representing turbulent vertical flux of longitudinal momentum, is presented in Figure 15c. A major tidal variation is obvious, with maxima at phases of strong tidal currents and a change in sign from flood to ebb time.

The turbulent salt flux terms, $\overline{u'S'}$ and $\overline{w'S'}$, are also shown in Figure 15. They again indicate a dependence on tidal flow. The longitudinal salt flux is approximately sinusoidal (because of the dominating u' part) and in phase with the vertical momentum flux. The vertical turbulent salt flux is not sinusoidal, but has pronounced maxima during ebb tide at the breakdown of the salinity stratification (see Figure 9). Except for the period at the end of the strong salinity stratification, the ratio $\overline{w'S'}/\overline{u'S'}$ is smaller than one similar to earlier results (West & Shiono, 1988).

Eddy-viscosity and eddy-diffusion coefficients

Parameterizations of turbulent momentum and salt fluxes are provided by the eddy viscosity and eddy diffusion coefficients. We attempted to determine these coefficients from quasi-simultaneous observations of turbulent fluctuations and of the slowly varying 'mean' gradients. We had to assume that the character of the fluctuations and the mean gradients did change sufficiently slowly over 50 m horizontally, the separation of the tripod and the profile measurements, to allow such a determination. Even then, with our data such an attempt was possible only for the vertical eddy viscosity A_z and the vertical and longitudinal eddy diffusion coefficients of salt D_z and D_x. These were obtained by using the following relationships:

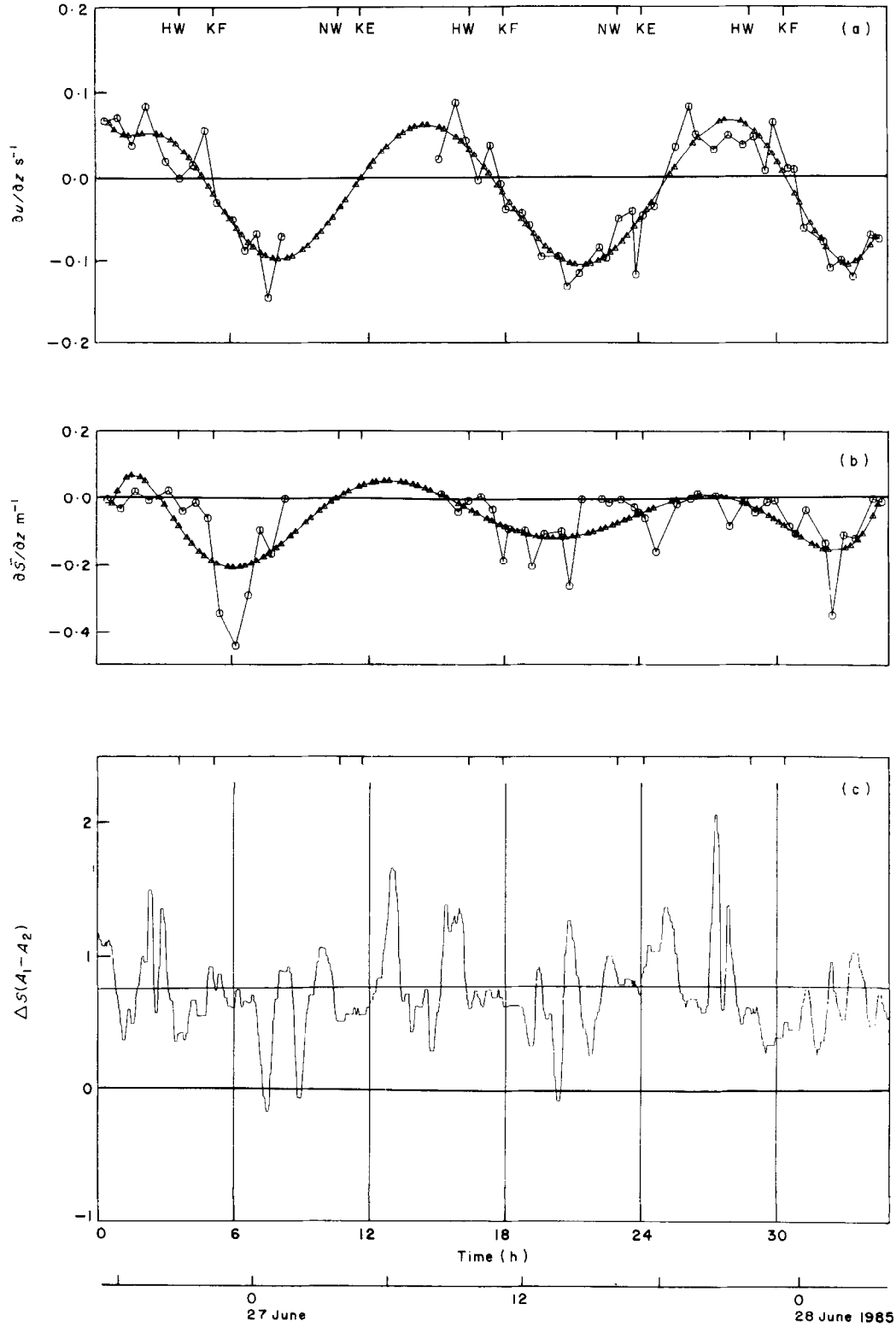

Figure 17. Time series of vertical gradients (a, b) of longitudinal current ($\partial u/\partial z$) and salinity ($\partial S/\partial z$) and salinity difference ΔS (Al–Al) between moorings A1 and A4 (c) (○, data; ▲, fit). For HW etc, see. Figure 7.

$$A_z = \frac{\overline{u'w'}}{\partial \bar{u}/\partial z}, \qquad D_z = \frac{\overline{w'S'}}{\partial \bar{S}/\partial z}, \text{ and} \qquad D_x = \frac{\overline{u'S'}}{\partial \bar{S}/\partial x}. \tag{4}$$

The vertical shear of the longitudinal current $\bar{u}$ was determined by the vertical-profiling instrument. The determination was restricted to the depth range of 1–4 m above the bottom. Pairs of down- and up-profiles were averaged and were fitted by least-squares with second-order polynomial. An example is given in Figure 16. $\partial u/\partial z$ was evaluated at 2·5 m above the bottom. The stress term $\overline{u'w'}$ was obtained from the tripod data at the same level.

Also, the tripod and profiling measurement periods alternated in time. But because the down- and up-profiles of vertical shear were averaged together and fit with a polynomial, the resulting shear profiles are likely well-representative of those for the periods of tripod observations. The result is presented in Figure 17a. The shear term changes sign during the tidal cycle, and the uncertainties in the calculation of A_z will increase considerably near the zero-crossings of $\partial \bar{u}/\partial z$. These critical periods were omitted from the calculations by removing data points with $\bar{u} < 0{\cdot}4$ m s^{-1} near slack water. The following results were then obtained by averaging the eddy coefficients over the half-tide periods between these low-velocity periods. We find a clear distinction between the vertical eddy viscosity coefficient A_z at flood and ebb time, with flood values of up to four times larger. Mean values are:

Flood time: $A_z = 7{\cdot}5 \times 10^{-3} \pm 4{\cdot}2 \times 10^{-3}$ m^2 s^{-1}
Ebb time: $A_z = 3{\cdot}3 \times 10^{-3} \pm 2{\cdot}0 \times 10^{-3}$ m^2 s^{-1}

The vertical eddy diffusion coefficient D_z for salt was determined correspondingly, with values deleted for a vertical salinity gradient below $-0{\cdot}05$ m^{-1}. As a result of a large variance of salinity gradient values compared to the mean gradients (see Figure 17b), particularly during flood conditions, the errors for D_z are larger than for A_z. Mean values are:

Flood time: $D_z = 1{\cdot}1 \times 10^{-3} \pm 15{\cdot}1 \times 10^{-3}$ m^2 s^{-1}
Ebb time: $D_z = 2{\cdot}2 \times 10^{-3} \pm 2{\cdot}2 \times 10^{-3}$ m^2 s^{-1}

It turns out that D_z is not significantly different from zero. The data are not sufficiently adequate for its accurate determination.

For a determination of D_x we need the longitudinal gradient of salinity. A calculation of this gradient was attempted by using the temperature/conductivity data from the moored instruments at Al and A4, which were 1130 m apart in the direction of the mean flow along a line about 150 m north of the isobath where the tripod was placed. Again, errors resulting from this separation of the tripod and the moored instrument line are assumed to be small. The salinity difference between Al and A4 is shown in Figure 17c. The mean gradient of $6{\cdot}6 \times 10^{-4}$ m^{-1}, indicated by the thin line, is used for the calculation of D_x. The resulting longitudinal eddy diffusion coefficient of salt varies from near-zero to approximately $1{\cdot}5$–$3{\cdot}5 \times 10^{-3}$ m^2 s^{-1} during parts of the flood period.

Conclusions

The aims of this study were specified in the introduction. The results can be summarized as follows: Acoustic-travel-time sensors proved to be appropriate devices for the measurement of turbulent flow in a tidal estuary. The spectra of 12·8 min pieces of the records have

properties in a central frequency range which are consistent with the $-5/3$ slope predicted by the Kolmogoroff theory of isotropic turbulence, but at higher frequencies indicate the transition to the much steeper slopes of the dissipative range. In some cases, surface wave signals dominated the turbulent signals. The time changes of total turbulent kinetic energy correlate well with the tidal current, with high correlation values for strong currents. However a retardation in the increase of turbulent energy after slack water by about one hour was found with respect to the tidal current increase.

Time series of the components of the Reynolds tensor and eddy diffusion vector displayed different characteristics. Variations in the diagonal terms of the Reynolds tensor, which are the turbulent energies, changed in phase almost sinusoidally with the tidal current. The vertical momentum flux term related to longitudinal flow also changed in phase with the tidal current, with a reversal of sign near high and low water. The vertical eddy diffusion term of salt displayed the same features. The longitudinal eddy diffusion term, however, did not change sinusoidally in time, but increased from low values to maxima during part of the ebb time.

Parameterization of eddy coefficients of vertical momentum flux (A_z) and longitudinal (D_x) salt transfer is possible in this study. Typical values are $A_z = 5 \times 10^{-3}\,\mathrm{m^2\,s^{-1}}$ and $D_x = 1 \times 10^{-3}\,\mathrm{m^2\,s^{-1}}$.

Acknowledgements

The project was funded by the GKSS-Research Center Geesthacht. The authors appreciated the encouragement by D. Bünemann and the assistance in data collection and processing by A. Müller, R. Riethmüller and U. Maixner, and by the crew of MS *Ludwig Prandtl*. During the analysis we have benefited from numerous discussions with H. Grassl and R. Riethmüller, and we appreciated the help of the staff of the Marine Physics Department of the Institut für Meereskunde at Kiel University in the data evaluation and the assistance of R. G. Peterson in the preparation of the manuscript.

References

Anwar, H. O. & Atkins, R. 1980 Turbulence measurements in simulated tidal flow. Journal of Hydraulics Division, ASCE, **106,** No. HY-8 Aug., 1273–1289.

Arge Elbe 1986. Das Abflußjahr 1985. Arbeitsgemeinschaft für die Reinhaltung der Elbe, 199 pp.

Barthel, V. 1985 Flachwasserseegang im Weserästuar. *Die Küste* **42,** 269–305.

Bendat, J. S. & Piersol, A. G. 1971 Random data: Analysis and measurement procedures. New York: Wiley Interscience, pp. 407.

Biermann, P. H., Diekmann, P. & Fedders, B. S. 1976 Die Telemetrie der Kieler Multisonde. *Interocean, Bd.* **II,** 1047–1055.

Bowden, K. F. & Howe, M. R. 1963 Observations of turbulence in a tidal current. *Journal of Fluid Mechanics,* 17, 271–284.

Fanger, H.-U., Kuhn, H., Maixner, U. & Milferstädt, D. 1979 Das hydrographische Meßsystem HYDRA. In: Das Bilanzierungsexperiment 1982 (BILEX 82) auf der Unterelbe, 17–44, (Hrsg.) W. Michaelis und H.-D. Knauth.

Flügge, G. 1982 Transport und Ausbreitungsmechanismen in Flüssen und Tideästuaren unter besonderer Berücksichtigung der Strömungsturbulenz. Mitt. Franz.-Inst., Sonderdruck aus Heft 55, pp. 118.

Grant, H. L., Stewart, R. W. & Moilliet, A. 1962 Turbulence spectra from a tidal channel. *Journal of Fluid Mechanics,* **12,** 241–263.

Gross, T. F. 1984 Tidal time dependence of geophysical turbulent boundary layer. Ph. D. Thesis University of Washington, University Ann Arbor, Michigan: Microfilms Intern., pp. 161.

Hinze, J. O. 1959 Turbulence. An Introduction to its mechanism and theory. New York: McGraw Hill, pp. 586.

Inoue, E. 1952 On the structure of wind near the ground. *Bulletin of the Institute of Agricultural Science,* **2,** Ser, A.

Koske, P. H., Krumm, H., Rheinheimer, G. & Szekielda, K. H. 1966 Untersuchungen über die Einwirkungen der Tide auf Salzgehalt, Schewbstoffgehalt, Sedimentation und Bakteriengehalt in der Unterelbe. *Kieler Meeresforschungen* **22,** 47–63.

Kroebel, W., Diehl, P., Ginzkey, L., Mahrt, K. H., Rathlev, J., Siara, R. & Schulz. Th. 1976 Die Kieler Multisonde der Jahre 1975/76. Ihre Sensoren, Parameter mit Ergebnissen von Datenaufnahme und Perspecktiven für ihre Auswertung. *Interocean, Bd.* **II,** 1034–1046.

Laufer, J. 1954 The structure of turbulence in fully developed pipe flow. National Advisory Committee for Aeronautics, USA, Technical Report **1174,** 10.

Lucht, F. 1964 Hydrographie des Elbe-Ästuars. *Archives d'Hydrobiologie,* **29** (Suppl.), 1–96.

Nakagawa, H., Nezu, I. & Ueda, H. 1975 Turbulence of open ocean channel flow over smooth and rough beds. *Proceedings of the Japanese Society of Civil Engineering,* **241,** 155–168.

Ohm, K. 1985 Optische Messungen zur Bestimmung von Schwebstofftransporten. *Die Küste,* **42,** 227–236.

Philips, O. M. 1958 The equilibrium range in the spectrum of wind-generated waves. *Journal of Fluid Mechanics,* **4,** 426–434.

Pierson, W. Jr. & Moskowitz, L. 1964. A proposed spectral form for fully-developed wind seas based on the similarity theory by S. A. Kitaigorodskii. *Journal of Geophysical Research,* **69,** 181–190.

Plate, E. 1974 Analyse kontinuierlicher Zufallsfunktionen. Institut für Wasserbau III, Karlsruhe Univ., Heft 1 der Mitteilungen, pp. 93.

Riethmüller, R., Schröder, M. & Maixner, U. 1985 Measurement of optical light attenuation profiles in the Elbe estuary. GKSS-Bericht, GKSS 85/E/58.

Rohde, H. 1971 Eine Studie über die Entwicklung der Elbe als Schiffahrts-Straße. *Mitt. Franzius Inst., Heft* **36,** 17–241.

Schauer, U. 1987 Determination of bottom boundary layer parameters at two shallow sea sites using the profile method. *Continental Shelf Research,* **7(10),** 1211–1230.

Schröder, M. 1987 Messung der turbulenten Impuls- und Salztransporte in der Mischungszone der Elbe, Ph.D. thesis. Berichte GKSS-Forschungszentrum Geesthacht GmbH. GKSS 87/E/16, pp. 190.

Seitz, R. C. 1973 Observations of intermediate and small scale turbulent water motion in a stratified estuary (Parts I and II). *Cheaspeake Bay Institute, Technical Report* **79,** Ref. 73–2, 158 + 89.

Shiono, K. 1981 Vertical turbulent exchange in stratified flow. Ph. D. thesis, Univ. of Birmingham, 127.

Siefert, W. 1975 Hydrologische Daten aus dem Tidegebiet der Elbe und ihrer Nebenflüsse. Hamburger Küstenforschung, Heft 35, 1–25.

Soulsby, R. L. 1977 Similarity scaling of turbulence spectra in marine and atmospheric boundary layers. *Journal of Physical Oceanography* **7,** 934–937.

Soulsby, R. L. 1980 Selecting record length and digitazation for near-bed turbulence measurements. *Journal of Physical Oceanography,* **10,** 208–219.

West, J. R. & Shiono, K. 1988 Vertical turbulent mixing processes on ebb tides in partially mixed estuaries. *Estuarine, Coastal and Shelf Science,* **26,** 51–66.

Wiseman, W. J. 1969 On the structure of high-frequency turbulence in a tidal estuary. *Chesapeake Bay Institute, Technical Report* **59,** Ref. 69–12, 77.